



**Cell-Directed Assembly of Lipid-Silica
Nanostructures Providing Extended Cell Viability**

Helen K. Baca, *et al.*
Science **313**, 337 (2006);
DOI: 10.1126/science.1126590

***The following resources related to this article are available online at
www.sciencemag.org (this information is current as of March 12, 2008):***

Updated information and services, including high-resolution figures, can be found in the online version of this article at:

<http://www.sciencemag.org/cgi/content/full/313/5785/337>

Supporting Online Material can be found at:

<http://www.sciencemag.org/cgi/content/full/313/5785/337/DC1>

This article **cites 25 articles**, 5 of which can be accessed for free:

<http://www.sciencemag.org/cgi/content/full/313/5785/337#otherarticles>

This article has been **cited by** 10 article(s) on the ISI Web of Science.

This article appears in the following **subject collections**:

Materials Science

http://www.sciencemag.org/cgi/collection/mat_sci

Information about obtaining **reprints** of this article or about obtaining **permission to reproduce this article** in whole or in part can be found at:

<http://www.sciencemag.org/about/permissions.dtl>

Cell-Directed Assembly of Lipid-Silica Nanostructures Providing Extended Cell Viability

Helen K. Baca,¹ Carlee Ashley,¹ Eric Carnes,¹ Deanna Lopez,¹ Jeb Flemming,² Darren Dunphy,² Seema Singh,² Zhu Chen,¹ Nanguo Liu,³ Hongyou Fan,² Gabriel P. López,¹ Susan M. Brozik,² Margaret Werner-Washburne,⁴ C. Jeffrey Brinker^{1,2,5*}

Amphiphilic phospholipids were used to direct the formation of biocompatible, uniform silica nanostructures in the presence of *Saccharomyces cerevisiae* and bacterial cell lines. The cell surfaces organize multilayered phospholipid vesicles that interface coherently with the silica host and help relieve drying stresses that develop with conventional templates. These host structures maintain cell accessibility, addressability, and viability in the absence of buffer or an external fluidic architecture. The cell surfaces are accessible and can be used to localize added proteins, plasmids, and nanocrystals. Prolonged cell viability combined with reporter protein expression enabled stand-alone cell-based sensing.

Living cells combine molecular recognition, amplification, and signal transduction in an extremely small “package,” making them ideally suited for miniaturized, stand-alone, environmental or physiological sensors. However, cellular integration into devices is problematic. Cells require functional bio/inorganic interfaces, benign synthesis conditions (1–3), and external fluidic support systems or immersion in buffer to avoid dehydration. Furthermore, as recently noted by Zhang (4), it is necessary to move beyond two-dimensional (2D) adhesion in dishes to 3D architectures that better represent the extracellular matrix, enabling cells to be surrounded by other cells, maintaining fluidic accessibility, and allowing development of 3D molecular or chemical gradients.

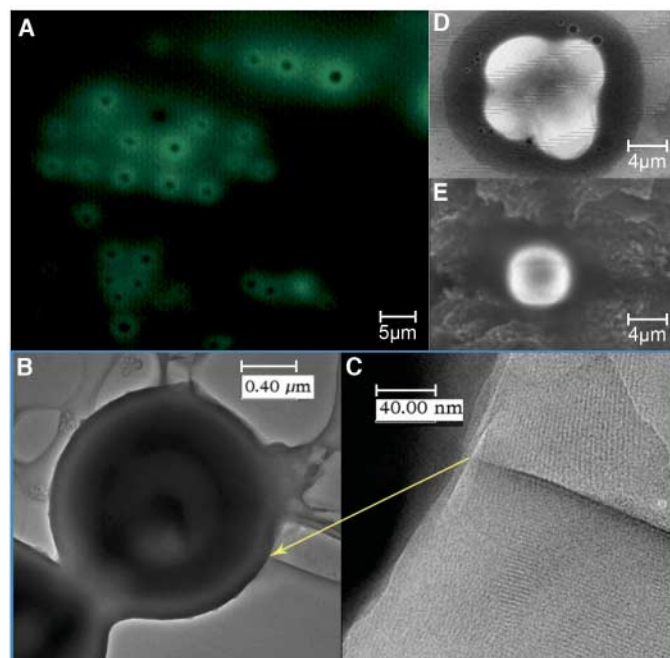
Although 3D cell immobilization in silica gels has been practiced for more than 15 years (5–12), shrinkage during drying creates stress in the silica network that causes cell lysis (13), and the nonuniform pore size leads to loss of fluidic connectivity (large pores dry out and isolate small water-filled pores). More specialized chemical vapor deposition and freeze-drying methods are effective in incorporating cells in silicate gels designed to avoid host-immune reactions or serve as bioreactors, but they also require maintenance in buffer or high humidity (14). Similar problems are encountered in other gel and polymer immobilization schemes, precluding their extended use under desiccating conditions. None of the approaches to date provide for bio/nano interfaces with 3D spatial control of structure and composition,

now recognized as important to the maintenance of natural cellular behavior patterns (15).

We have adapted our evaporation-induced self-assembly (EISA) approach (16) to incorporate cells in a uniform, biocompatible silica nanostructure, using standard unit operations like spin- or dip-coating, ink-jet printing, or molding [fig. S1 (17)]. In this case, the nanostructured host, composed of nanometer-scale channels with a narrow size distribution, prevents extensive drying and associated stresses (18, 19) and maintains 3D fluidic connectivity. The evaporation-driven immobilization procedures also allow facile cellular integration into devices.

Fig. 1. *S. cerevisiae* organize a lipid-rich shell that interfaces coherently with the surrounding nanostructured silica host.

(A) Confocal fluorescence image of immobilized cells with 1% substitution of the fluorescently labeled lipid analog, 1-hexanoyl-2-[6-[(7-nitro-2-1,3-benzoxadiazol-4-yl)amino]hexanoyl]-sn-glycero-3-phosphocholine (diC_6 PC-NBD). Brighter areas indicate preferential concentration of lipid around cells compared to the surrounding lipid/silica host matrix. (B and C) TEM images of cell immobilized within nanostructured lipid/silica matrix by spin-coating directly on holey carbon-coated copper grid. (D and E) SEM of cells immobilized in silica host prepared with (D) and without (E) lipids. The dark region around the cells in (D) corresponds to an area of high carbon/phosphorus concentration consistent with the presence of lipids (fig S2). In (E), the dark region is a crevice. Cells are firmly immobilized only when the lipid interface is present. In the absence of lipid, cell washout occurs and film cracking is prevalent.



¹Department of Chemical and Nuclear Engineering, University of New Mexico, ²Sandia National Laboratories, Albuquerque, NM 87185, USA. ³Los Alamos National Laboratory, Chemistry Division, Los Alamos, NM 87545, USA. ⁴Department of Biology, ⁵Department of Molecular Genetics and Microbiology, University of New Mexico, Albuquerque, NM 87131, USA.

*To whom correspondence should be addressed. E-mail: cjbrink@sandia.gov

As we have shown using in situ grazing incidence small-angle x-ray scattering (GISAXS) (20), during EISA, solvent evaporation (typically water-ethanol) concentrates the dissolved silica and surfactant, which causes micelles to form and progressively assemble into 3D silica-surfactant mesophases. However, surfactants used to date in EISA, and more generally in templated mesoporous silicas (21), are detergent monomers that insert into cell membranes and lead to their solubilization, inducing rapid cell death. Thus, we replaced standard surfactants with phospholipids, which are integral components of the cell membrane. Through extensive GISAXS and cell-viability studies, we identified diacylphosphatidylcholines (diC_n PC), with zwitterionic head groups and short, double acyl tails ($n = 6$ to 10), as having minimal disruptive electrostatic interactions with cell membranes and as being water soluble with sufficiently small critical packing parameters g (22–24) to direct the formation of high-curvature 3D (hexagonal or cubic) lipid-silica mesophases. [For details on lipid-directed assembly of silica mesophases, see (17).]

Using diC_n PC as a structure-directing agent, we find that increasing diC_n PC/silica ratios cause the final silica mesostructure to progress from wormlike to hexagonal to cubic to lamellar phases in a manner similar to that reported by us previously for standard surfactants (25). However, the addition of stationary-phase *Saccharomyces cerevisiae* at concentrations >10 wt% markedly alters the lipid-silica self-assembly pathway in several respects. Laser-scanning confocal imaging

of systems prepared with 1% substitution of a fluorescently labeled lipid analog showed that, during EISA, cells rapidly organized around themselves a lipid-rich shell with nearly uniform

thickness of $\sim 2 \mu\text{m}$ (Fig. 1A). Elemental mapping indicated that this shell largely excludes silica (fig. S2) (17), and fluorescence recovery after photo-bleaching (FRAP) experiments show

that this lipid-rich region remains fluid for several hours after the EISA process. Corresponding FRAP experiments performed on the surrounding host matrix, where the lipid is confined within a partially solidified silica nanostructure, show no measurable fluorescence recovery.

Direct transmission electron microscopy (TEM) imaging and scanning electron microscopy (SEM) (Fig. 1, B to E) show that the lipid

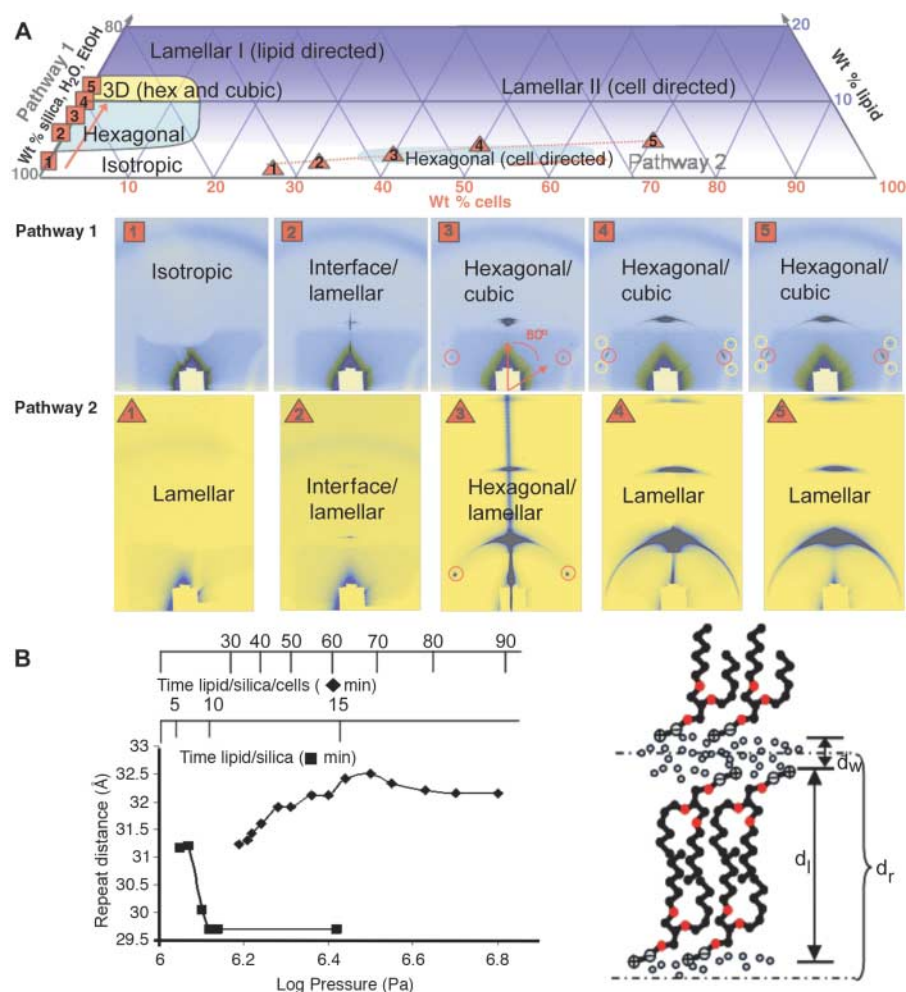


Fig. 2. Structural development in systems containing cells and cell surrogates. (A) Compositional space for lipid-directed (red squares, Pathway 1) and cell-directed assembly (red triangles, Pathway 2) with time-resolved GISAXS images showing structure development for the evolving systems. Films were cast remotely in a humidity-controlled chamber and probed in a horizontal geometry. Weight loss during solvent evaporation was measured to relate structural evolution to film composition. The evaporation-induced compositional trajectories are mapped onto a ternary diagram with vertices representing the weight percent of aqueous silica/solvent, lipid, and wet cells in the system. During lipid-directed assembly (Pathway 1), the film is initially isotropic (panel 1), with the first sign of order appearing as a Bragg reflection in the specular direction (panel 2), representing short-range lamellar ordering parallel to the substrate surface. This phase, which typically nucleates at the vapor/liquid interface, disappears as Bragg spots with sixfold symmetry appear, indicating the presence of a bulk 2D hexagonal phase (panel 3). The final phase is a mixture of 2D hexagonal and other 3D phases (panels 4 and 5). With cell-directed assembly (Pathway 2), the film is again initially isotropic (panel 1). A lamellar phase appears in panel 2 and persists throughout the self-assembly process (panels 3 to 5). The hexagonal phase in panel 3 disappears, and the end point is a global lamellar phase. (B) Progression of repeat distance for systems during EISA as a function of time and evolving osmotic pressure for lipid-silica (■) and lipid-silica-cell systems (◆). The repeat distance (d_r) is measured from in situ 2D GISAXS images with Bragg reflections in the specular direction. It includes the fluid interbilayer space (d_w) and the lipid bilayer (d_l) and is initially the same (31 Å) in the lamellar phase that forms first in both systems. We propose that with cells, the increase in repeat distance results from an increasing lipid bilayer thickness due to reduced interdigitation and lipid reorientation. Osmotic pressure Π is calculated from the concentration of all osmolytes [according to $\Pi = cRT$, where c is concentration ($\text{mol}\cdot\text{m}^{-3}$), R is the gas constant ($\text{J}\cdot\text{K}^{-1}\cdot\text{mol}^{-1}$), and T is temperature (K)] in the bulk solution, as determined from in situ gravimetric analysis of the evaporating system.

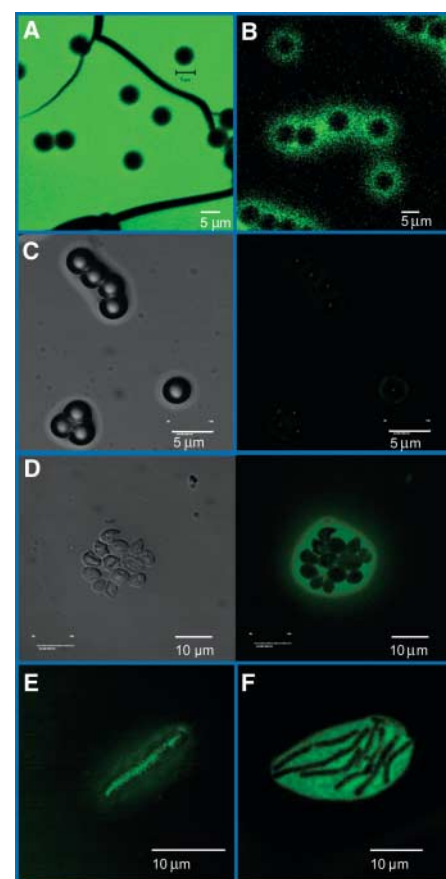


Fig. 3. Chemical gradient development during cell-directed assembly. (A) Fluorescently labeled lipid added with neutral latex beads (compare to Fig. 1A). Lipid is dispersed evenly throughout the sol, with no aggregation at the surface, consistent with the observation that uncharged beads have no influence on self-assembly. (B) Lipid aggregates inhomogeneously at the surface of charged beads, indicating that electrostatic interactions promote lipid accumulation. (C) Differential interference contrast (DIC) (left) and fluorescence images (right) of negatively charged beads with 2',7'-difluorofluorescein (Oregon Green 488) added during EISA. The DIC images locate the beads, whereas the fluorescence reports the local pH. The uniform low fluorescence corresponds to the pH observed for lipid/silica systems (D) far from the cells. (D) Lipid-silica system with *S. cerevisiae*. The bulk pH (dark area) is ~ 3 , whereas the local pH surrounding the cells is ~ 5 to 6. (E) Fluorescently labeled lipid aggregates at surface of *Bacillus subtilis*. (F) *B. subtilis* mediates local pH in a manner similar to that of *S. cerevisiae*.

shell maintains a coherent interface between the cell and the adjoining silica nanostructure that withstands drying and evacuation to 10^{-8} Pa during electron imaging while preserving cell viability (26). By comparison, *S. cerevisiae*-silica films prepared identically, but without lipid, develop macroscopic cavities (Fig. 1E) around the cells because of drying stresses. Such stresses are absent in the corresponding lipid-containing systems [see (17) and discussion below].

In addition to locally modifying their environments, *S. cerevisiae* globally alter the sequence of mesophase development during EISA. By performing in situ 2D GISAXS experiments on evaporating lipid-silica films with and without *S. cerevisiae* (17), we determined that a system that would ultimately form a 3D hexagonal/cubic mesophase prepared without yeast (Fig. 2A, pathway 1) evolves from an isotropic phase through intermediate lamellar and mixed lamellar/2D hexagonal mesophases to a final lamellar mesophase (Fig. 2A, pathway 2) when prepared with 27 wt% wet cells.

Although the mesophases are oriented with respect to the substrate surface in both cases, the repeat distances of the evolving mesophases differ markedly (Fig. 2B). With cells present, the d -spacing normal to the substrate increases throughout the course of EISA. This behavior is contrary to that observed generally in EISA (20) and specifically here in the system without cells, where dehydration and silica condensation cause a decrease in d -spacing.

These cellular influences on inorganic self-assembly can be contrasted with the situation when spherical colloidal particles are added to surfactant-silica systems—these particles have no influence on self-assembly (27). Unlike latex beads, cells are active colloids, where the cell wall is a dynamic structure, actively maintained by the living cell (28, 29) and capable of sensing and responding to its environment. We compared structural and chemical development in systems

containing yeast to surrogate systems in which cells were replaced with comparable volume fractions of uncharged or negatively charged latex beads. Confocal fluorescence images show that while cells accumulate a coherent lipid interface (Fig. 1A), no lipid aggregation occurs around the neutral bead surface (Fig. 3A). Lipid aggregation around negatively charged beads, although less homogeneous (Fig. 3B), implies that electrostatic interactions are responsible in part for forming the lipid-rich interface in cell-containing systems.

More pronounced are distinctions noted when probing local chemical effects. Fluorescence imaging of systems containing uncharged or negatively charged beads and an impermeant pH-sensitive dye shows that the film has a uniform pH of ~ 3 , attributed to the acidity of the silanol-terminated silica surface (Fig. 3C). In contrast, with cell-containing films, we observe a local pH of 5 to 6 at the cell surface that decreases to about 3 to 4, corresponding to the nanostructured silica matrix, at a distance of several micrometers (Fig. 3D). Time-resolved studies indicate that these very different pH conditions are maintained throughout the course of EISA.

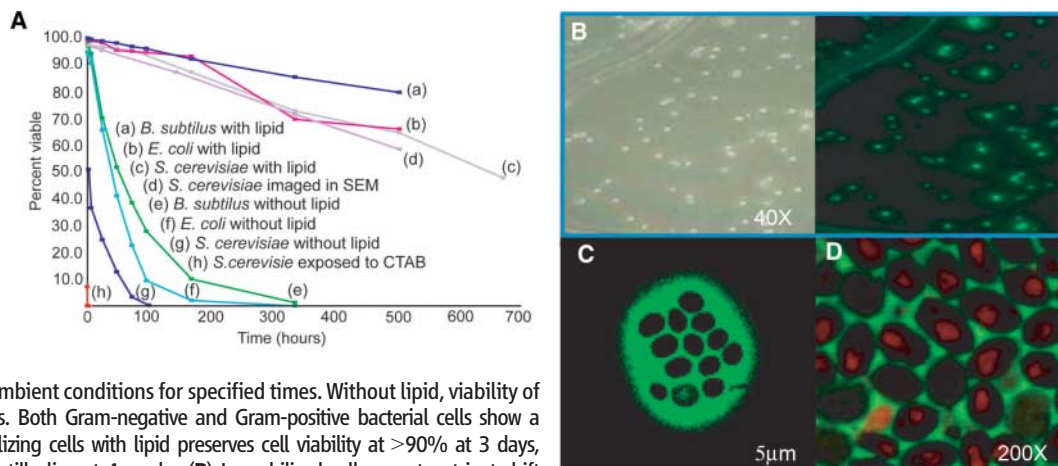
We rationalize the cell's influence on its local and global environments by considering its response to the evolving chemical and physical conditions of EISA. As solvent evaporates, the concentration of osmolytes in the system increases. Unlike latex beads, stationary-phase cells can release up to 35% of their cellular water volume (30) in response to a change in turgor pressure in the cell membrane, which would increase the volume of water in the surrounding lipid shell of ~ 2 - μm thickness by more than 60%. The resulting pH gradient that develops around the cell in turn affects both the local lipid interface and the host lipid/silica matrix.

The pH of ~ 5 in the immediate vicinity of the cell facilitates adsorption of a lipid layer on the cell surface; both $d1C_n$ PC and the cell wall are near their isoelectric points, where comple-

mentary interactions between dipoles on the lipid head group, and discrete positive and negative surface charges, will be enhanced (fig. S3) (17). Dipole-dipole interactions between head groups, and van der Waals interactions between alkane tails, promote the further aggregation of lipid bilayers into the ordered lamellar structure that appears rapidly in the sequence of GISAXS patterns (Fig. 2A). Far from the cells, a bulk 2D hexagonal phase develops on a longer time scale commensurate with that of the EISA process. This initial hexagonal phase (Fig. 2A, pathway 2, panel 3) is transient. During the later stages of EISA, it disappears through transformation to a lamellar mesophase with d -spacing corresponding to that of the lipid bilayers. Based on the coherent, seamless nature of the lipid-silica interface (Fig. 1), we suppose that the transformation initiates at this lipid interface because of charge matching with the high density of dipoles on the PC bilayers, and proceeds through the bulk system, giving the final global lamellar mesophase seen in Fig. 2A, pathway 2.

The pH gradient also determines the extent of silica incorporation in the lipid interface and the dimensional scale of the self-assembling lipid and silica nanostructures. The higher pH in the vicinity of the cell greatly enhances the silica condensation rate there and provides a kinetic barrier to diffusion of silica oligomers that effectively excludes silica from the immediate lipid-rich environment of the cell [see quantitative elemental analysis, fig. S2 (17)]. Based on combined in situ GISAXS and gravimetric analyses, we plot in Fig. 2B the measured repeat distance of the nanostructure as it varies with time and developing osmotic pressure during EISA. For lipid-silica systems without cells, EISA proceeds with a progressive reduction in d -spacing resulting from dehydration and silica condensation. However, for films containing cells, d increases both by expulsion of water

Fig. 4. (A) Viability of stationary-phase cells immobilized with and without lipid. Viability of *S. cerevisiae* is assessed with a two-color fluorescent probe that is incorporated into cellular intravacuolar structures by metabolically active cells. The dye undergoes an adenosine 5'-triphosphate-dependent change in fluorescence from green to red as it is transported from the cytosol to vacuoles. Bacterial cell viability is measured by means of a nucleic acid stain. Films are exposed to the buffered probe after aging at ambient conditions for specified times. Without lipid, viability of *S. cerevisiae* drops to 50% at 2 hours. Both Gram-negative and Gram-positive bacterial cells show a similar rapid drop in viability. Immobilizing cells with lipid preserves cell viability at $>90\%$ at 3 days, with more than 50% of *S. cerevisiae* still alive at 4 weeks. **(B)** Immobilized cells report nutrient shift through GFP expression after film-drying times of 24 hours. DIC image (left) identifies cell location, and fluorescence image (right) shows GFP expression by viable cells. **(C)** Optically labeled (2% NBD label) lipid-coated gold nanocrystals are concentrated at the cell surface after 6 hours while maintaining viability. **(D)** Lipid-coated CdSe nanocrystals are rapidly concentrated at the cell surface and internalized at 24 hours, as noted by red fluorescence from within cells. Labeled lipid (green, $d1C_6$ PC-NBD) concentrates around the cell.



from the cells, which helps maintain the interbilayer thickness (d_w in Fig. 2B), and through an increase in the bilayer thickness (d_l in Fig. 2B). d_l increases because the higher local pH deprotonates lipid head groups, which decreases their optimal surface area. To avoid water contact at the head group/hydrocarbon interface, lipid tails reorient toward configurations more normal to the interfacial planes (31, 32).

In addition to chemical stresses, we anticipated that the immobilized cells could sense and respond to mechanical stresses that arise during drying and condensation of the inorganic network (and are known to cause cell lysis in other immobilization schemes). However, as shown in fig. S4 (17), where we plot biaxial stress measured in situ using a cantilever beam, cell-directed assembly proceeds at a state of nearly zero stress, which likely accounts for its unusual biocompatibility (see discussion below). In comparison, without cells, and without cells and lipid, drying-induced shrinkage creates biaxial tensile stresses. This difference is attributed in part to the lamellar nanostructure that mechanically decouples each successive layer in the direction normal to the substrate surface. Stress may also be mitigated by the compensatory effects of water production and increased d -spacing resulting from the cell's response to hyperosmotic stress.

The cell-directed assembly process we describe creates a highly biocompatible environment for immobilized cells. Using live-dead viability probes, we determined the viability of cells maintained without buffer at ambient temperature and humidity. We compare results for cells immobilized by using cell-directed assembly to systems containing silica alone or silica plus a standard surfactant in Fig. 4A. Immobilized within silica alone, >50% of *S. cerevisiae* cells were dead within 2 hours, whereas exposure to a typical detergent resulted in immediate cell death. In comparison, >50% of the cells were viable after 4 weeks when immobilized in lipid-silica hosts. Even after SEM imaging, 60% of the cells were viable at 3 weeks.

The phospholipid interface contributes to this enhanced cell viability in several other ways. It minimizes cytotoxic electrostatic and hydrogen bonding interactions between the silica host and cell surface phospholipids (33). The zwitterionic PC head groups also avoid strong electrostatic binding interactions with the cell that are typical of positively charged surfactants, such as cetyltrimethylammonium bromide (CTAB), which immediately lyse the cell membrane (Fig. 4A). Wedge-shaped surfactants in general, including short-chained d_iC_n PCs, will distribute into the outer leaflet of the cell membrane, inducing tension and causing eventual destabilization (34). During cell-directed assembly, however, the immediate incorporation of lipids in a multilamellar mesophase reduces the concentration of monomers in the vicinity of the cell available for insertion. Finally, as confirmed by weight-loss

measurements and in situ attenuated total reflection Fourier transform infrared (ATR-FTIR) spectroscopy, the hygroscopic nature of the PC lipids and their organization into a uniform nanostructure serve to suppress overall water loss, allowing the cell to be maintained in a fluid, water-rich microenvironment.

We used *S. cerevisiae* as a model eukaryotic sensor based on reporter protein expression. Yeast cells were genetically modified with plasmids designed to express green fluorescent protein (GFP) regulated by the *GAL1* promoter (35) and immobilized by cell-directed assembly. Although previously reported induction of GFP expression in immobilized *Escherichia coli* required short film-drying times of 40 min or less to prevent cell inactivation (5, 13), we induced GFP expression in response to a glucose-to-galactose nutrient shift in films that were exposed to dry, ambient conditions for >24 hours (Fig. 4B). For samples provided to an external collaborator, GFP expression was induced in immobilized cells stored dry for >6 months at 4°C (36). Hyperspectral imaging (37) of GFP expression in immobilized cells confirmed the potential for use in array technologies and individual addressability of cells.

Variations in both cell surface characteristics and the cellular response to osmotic stress could cause the cell-directed assembly process to be cell-specific. However, Fig. 3, E and F, show that for Gram-positive bacterium *Bacillus subtilis*, both lipid aggregation and pH mediation occur in a manner similar to that for *S. cerevisiae*. In addition, Fig. 4A shows comparable levels of viability for *S. cerevisiae*, *B. subtilis*, and Gram-negative bacterium *E. coli*.

These scaffolds formed through cell-directed assembly also allow construction of hierarchical structures in which additional components are selectively localized at the cell surfaces (fig. S5). Confocal microscopy of systems containing fluorescently labeled bovine serum albumin, or the transmembrane protein bacteriorhodopsin (fig. S5) (17), demonstrate the selective incorporation of proteins in the naturally fluidic lipid environment surrounding *S. cerevisiae*. Retention of protein conformation, a challenge in localizing transmembrane proteins, may be assisted by modulation of interface fluidity and curvature through variation of lipid chain length and incorporation of fatty acids or cholesterol into the bilayers. For *E. coli* systems that incorporate plasmid vectors designed for GFP expression, plasmid localization at the cell interface enables highly efficient transformation and reporter protein expression (fig. S5) (17). Finally, Fig. 4, C and D, show immobilized cells prepared with lipid-stabilized Au or CdSe nanocrystals (38). The nanocrystals are rapidly organized at the cell surface and mainly internalized after 24 hours.

References and Notes

1. M. Tirrell, E. Kokkoli, M. Biesalski, *Surf. Sci.* **500**, 61 (2002).
2. R. Langer, D. A. Tirrell, *Nature* **428**, 487 (2004).

3. R. F. Service, *Science* **297**, 962 (2002).
4. S. G. Zhang, *Nat. Biotechnol.* **22**, 151 (2004).
5. J. R. Premkumar et al., *Chem. Mater.* **14**, 2676 (2002).
6. E. Pope, *J. Sol-Gel Sci. Technol.* **4**, 225 (1995).
7. S. Y. Chia, J. Urano, F. Tamanoi, B. Dunn, J. I. Zink, *J. Am. Chem. Soc.* **122**, 6488 (2000).
8. N. Nassif et al., *Nat. Mater.* **1**, 42 (2002).
9. A. Coiffier, T. Coradin, C. Roux, O. M. M. Bouvet, J. Livaige, *J. Mater. Chem.* **11**, 2039 (2001).
10. J. F. T. Conroy et al., *J. Sol-Gel Sci. Technol.* **18**, 269 (2000).
11. I. Gill, A. Ballesteros, *J. Am. Chem. Soc.* **120**, 8587 (1998).
12. L. Inama, S. Dire, C. G. A. Cavazza, *J. Biotechnol.* **30**, 197 (1993).
13. M. L. Ferrer, L. Yuste, F. Rojo, F. del Monte, *Chem. Mater.* **15**, 3614 (2003).
14. H. Bottcher, U. Soltmann, M. Mertig, W. Pompe, *J. Mater. Chem.* **14**, 2176 (2004).
15. M. Stevens, *Science* **310**, 1135 (2005).
16. C. Brinker, Y. Lu, A. Sellinger, H. Fan, *Adv. Mater.* **11**, 579 (1999).
17. Materials, methods, and supporting material are available on Science Online.
18. Above several % relative humidity, hydrophilic channels <5 nm in diameter remain fully saturated.
19. A. P. Malanoski, F. van Swol, *Phys. Rev. E* **66**, 041602 (2002).
20. D. A. Doshi et al., *J. Am. Chem. Soc.* **125**, 11646 (2003).
21. C. Kresge, M. Leonowicz, W. Roth, J. Vartuli, J. Beck, *Nature* **359**, 710 (1992).
22. The packing parameter $g = [v/(a-l)]$ describes the geometric packing of amphiphilic molecules as a function of their head-group area (a), hydrocarbon chain volume (v), and critical chain length (l) and predicts the structures they form. For double-chained lipids, the glycerol backbone extends in the direction of the head-group chain, displacing the relative length of the two acyl chains by about three methylene groups and requiring a correction in l of ~4 Å.
23. J. Israelachvili, *Intermolecular and Surface Forces* (Academic Press, San Diego, ed. 2, 1992).
24. J. H. Kleinschmidt, L. K. Tamm, *Biophys. J.* **83**, 994 (2002).
25. Y. F. Lu et al., *Nature* **389**, 364 (1997).
26. For TEM imaging, lipid/silica/cell systems were spin-coated directly on a holey carbon-coated copper grid without fixative treatment for simultaneous visualization of cells and silica. Cell viability was assessed for cells exposed to 20 μ A at 1 kV and 10^{-8} -Pa vacuum for 5 min during SEM imaging.
27. P. Yang et al., *Science* **282**, 2244 (1998).
28. F. Klis, M. P. K. Hellingwerf, S. Brul, *FEMS Microbiol. Rev.* **26**, 239 (2002).
29. G. Smits, J. Kapteyn, H. van den Ende, F. Klis, *Curr. Opin. Microbiol.* **2**, 348 (1999).
30. I. M. deMaranon, P. A. Marechal, P. Gervais, *Biochem. Biophys. Res. Commun.* **227**, 519 (1996).
31. D. A. Doshi et al., *J. Phys. Chem. B* **107**, 7683 (2003).
32. J. F. Nagle, S. Tristram-Nagle, *Biochim. Biophys. Acta Rev. Biomembr.* **1469**, 159 (2000).
33. N. Sahai, *J. Colloid Interface Sci.* **252**, 309 (2002).
34. H. Hauser, *Biochim. Biophys. Acta* **1508**, 164 (2000).
35. Yeast strains (mww966) with a μ 2 pYES2plasmid containing the *GAL1* promoter fused to the GFP coding sequence were used for reporter protein expression.
36. *S. cerevisiae* cells supplied by the Naik Lab (R. Naik, Air Force Research Laboratory, Wright Patterson AFB) were immobilized by cell-directed assembly and stored dry at 4°C. GFP expression was induced with a 60-min exposure to minimal media lacking arginine.
37. M. B. Sinclair, J. A. Timlin, D. M. Haaland, M. Werner-Washburne, *Appl. Opt.* **43**, 2079 (2004).
38. H. Y. Fan et al., *Science* **304**, 567 (2004).
39. H.K.B. acknowledges support through the National Defense Science and Engineering Graduate Fellowship Program sponsored by the Air Force Office of Scientific Research (AFOSR). C.J.B. acknowledges support from AFOSR (FA9550-04-1-0087), the U.S. Department of Energy Basic Sciences Program, the Sandia National

Laboratories Laboratory Directed Research and Development program, the Army Research Office (DAAD 19-03-1-227), and the NIH Nanomedicine Center Program (#206-00139-06). We acknowledge P. Calvert for discussions of ink-jet printing. Images in this paper were generated in the University of New Mexico Cancer Center Fluorescence Microscopy Facility, supported as detailed at <http://kugrserver.health.unm.edu:16080/microscopy/>

facility.html. Use of the Advanced Photon Source was supported by the U.S. Department of Energy, Office of Science, Office of Basic Energy Sciences, under Contract No. W-31-109-ENG-38. Sandia is a multiprogram laboratory operated by Sandia Corporation, a Lockheed Martin Company, for the U.S. Department of Energy's National Nuclear Security Administration under Contract DE-AC04-94AL85000.

Supporting Online Material

www.sciencemag.org/cgi/content/full/313/5785/337/DC1
Materials and Methods
Figs. S1 to S5
References

23 February 2006; accepted 1 June 2006
10.1126/science.1126590

Mode Locking of Electron Spin Coherences in Singly Charged Quantum Dots

A. Grelich,¹ D. R. Yakovlev,^{1,2*} A. Shabaev,^{3,4} Al. L. Efros,^{3*} I. A. Yugova,^{1,5} R. Oulton,¹ V. Stavarache,⁶ D. Reuter,⁶ A. Wieck,⁶ M. Bayer^{1*}

The fast dephasing of electron spins in an ensemble of quantum dots is detrimental for applications in quantum information processing. We show here that dephasing can be overcome by using a periodic train of light pulses to synchronize the phases of the precessing spins, and we demonstrate this effect in an ensemble of singly charged (In,Ga)As/GaAs quantum dots. This mode locking leads to constructive interference of contributions to Faraday rotation and presents potential applications based on robust quantum coherence within an ensemble of dots.

Electron spins in ensembles of quantum dots (QDs) offer one possible pathway to implementing quantum information technologies in a solid-state environment (1–4). Unfortunately, inhomogeneities within an ensemble lead to the rapid loss of coherence among the phases of the spins, typically on the scale of nanoseconds (5–7). This is orders of magnitude shorter than the coherence time for a single QD, which can be as long as microseconds (8). Theoretically, the single-spin coherence time can be even longer, in principle up to twice the spin relaxation time (9), which is on the scale of milliseconds (10, 11). The fast dephasing in an ensemble is due to both spatial fluctuations in the nuclear magnetic fields (12, 13) and inhomogeneities in the electron g factor (3). These effects may be overcome by sophisticated spin-echo techniques (14), but a simple and robust technique for preserving spin coherence could ultimately enable many of the operations that are critical to the processing of quantum information, including initialization, manipulation, and read-out of a coherent spin state.

Here we report an optical technique based on time-resolved Faraday rotation (FR) measurements of the electron spin dynamics in an ensemble of QDs to recover the coherence time

of a single QD. A periodic train of circularly polarized light pulses from a mode-locked laser synchronizes the precession of the spins to the laser repetition rate, transferring the mode-locking into the spin system. This synchronization leads to constructive interference of the electron spin polarization in time. The interference also gives the possibility for all-optical coherent manipulation of spin ensembles: The electron spins can be clocked by two trains of pump pulses with a fixed temporal delay. After this pulse sequence, the QD ensemble shows multiple echo-like FR signals with a period equal to the pump pulse separation.

The experiments were performed on self-assembled (In,Ga)As/GaAs QDs prepared such that each dot contains on average a single electron (16) [Supporting Online Material (SOM) Text]. The full width at half maximum of the photoluminescence emission line is 15 meV (Fig. 1B). We used a mode-locked laser that emits pulses with 1.5-ps duration at a rate of 75.6 MHz, corresponding to a pulse separation of $T_R = 13.2$ ns. In the pump-probe FR with picosecond resolution, spin coherence is generated by a circularly polarized pump pulse, and this coherence is monitored through the precession of the spins about a magnetic field that is applied perpendicular to the structure growth axis (Fig. 1A). For this monitoring, a subsequent linearly polarized probe pulse is used; the beam polarization is rotated due to circular birefringence of the dots that is induced by the photogenerated spin polarization (SOM Text).

In Fig. 1C, FR signals of the QDs are shown as a function of delay between pump and probe at different magnetic fields B . At $B = 0$, a single, strongly damped oscillation is seen at positive delays after the pump pulse arrival at

time $t = 0$. This signal arises from light scattering by the spin-polarized photoinduced carriers, which together with the residual electron form a negatively charged exciton (trion). No signal is detected at negative delays ($t < 0$). In a magnetic field of 1 T, long-lived electron spin quantum beats appear at positive delays. From the weak decay of the FR signal with increasing delay, a spin dephasing time T_2^* of up to 2 ns can be estimated at low fields. Because this time is much longer than the 400-ps lifetime of the electron-hole pairs injected by the pump pulse (15), the beats are due to the spin precession of the residual electrons in the QDs with a frequency $\omega_e = g_e \mu_B B / \hbar$, where μ_B is the Bohr magneton and \hbar is Planck's constant divided by 2π . $|g_e| = 0.57$ is the electron g factor (16). For a magnetic field of 6 T, an additional modulation of the FR signal appears at short positive delays, whose decay during 400 ps matches the electron-hole lifetime. This modulation arises from interference of spin precessions of the residual electron and the photoexcited carriers (16).

The long-lived beats in the FR signal at positive delays are due to initialization of spin coherency of the residual QD electrons by the pump pulses that are resonant with the trion. If the electron spin precession is slow in the limit of weak or zero magnetic field such that $\omega_e \tau_e \ll 1$, where τ_e is the trion lifetime, then the coherency is nullified after trion recombination (16–18). In the opposite case of fast spin precession ($\omega_e \tau_e \gg 1$), the spin coherence is controlled by the pump pulse area (16). For that situation, Rabi-oscillations of the FR amplitude have been reported for the studied structures (16) for which the residual electron spin coherence reaches maximum for pulses with area π .

Under these conditions, strong spin quantum beats with a frequency corresponding to the electron precession are observed also at negative delays in a nonzero magnetic field. The amplitude of these quantum beats increases when approaching zero delay $t = 0$. Spin beats at negative delay have been reported for experimental situations in which the decay time exceeds the time interval between the pump pulses: $T_2^* \geq T_R$ (3). This is clearly not the case here, where the FR signal has fully vanished after 1.2 ns at $B = 6$ T, so that $T_2^* < T_R$.

The FR traces were analyzed for positive and negative delays by exponentially damped oscillatory functions. The magnetic field dependencies of the decay time T_2^* of the ensemble spin precession are given in Fig. 1D. The varia-

¹Experimentelle Physik II, Universität Dortmund, D-44221 Dortmund, Germany. ²A. F. Ioffe Physico-Technical Institute, 194021 St. Petersburg, Russia. ³Naval Research Laboratory, Washington, DC 20375, USA. ⁴School of Computational Sciences, George Mason University, Fairfax, VA 22030, USA. ⁵Institute of Physics, St. Petersburg State University, 198504, St. Petersburg, Russia. ⁶Angewandte Festkörperphysik, Ruhr-Universität Bochum, D-44780 Bochum, Germany.

*To whom correspondence should be addressed. E-mail: dmitri.yakovlev@physik.uni-dortmund.de (D.R.Y.); efros@dave.nrl.navy.mil (A.L.E.); manfred.bayer@physik.uni-dortmund.de (M.B.)